Chapter 4

Radio astronomy fundamentals

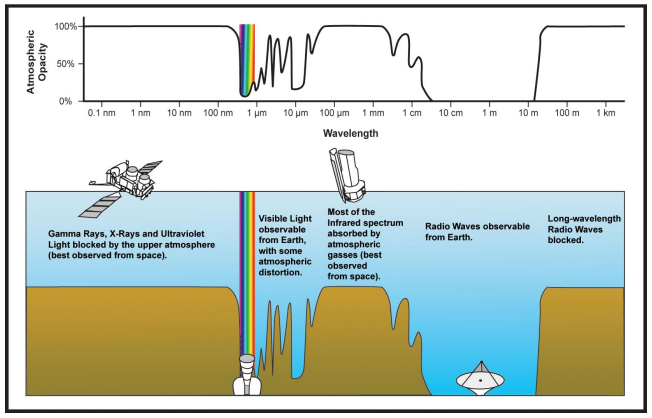

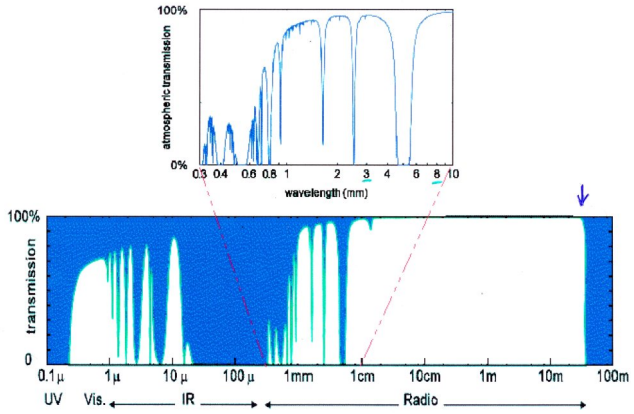

4.1 Radio telescopes

Tuorla 2-meter solar radio telescope

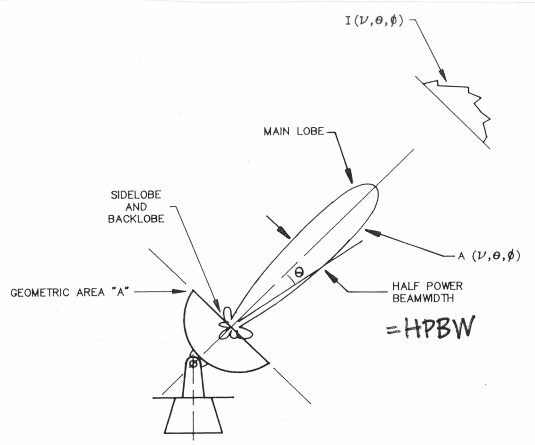

Figure 3–2. The reception pattern of an antenna.

Figure 4.1: HPBW 'half power beam width', FWHM 'full width half maximum', true (efficient) antenna area = aperture efficiency $\eta \times$ geometric area. η varies $\approx 0.3 - 0.7$. Surface accuracy of the dish has to be better than the wavelength used.

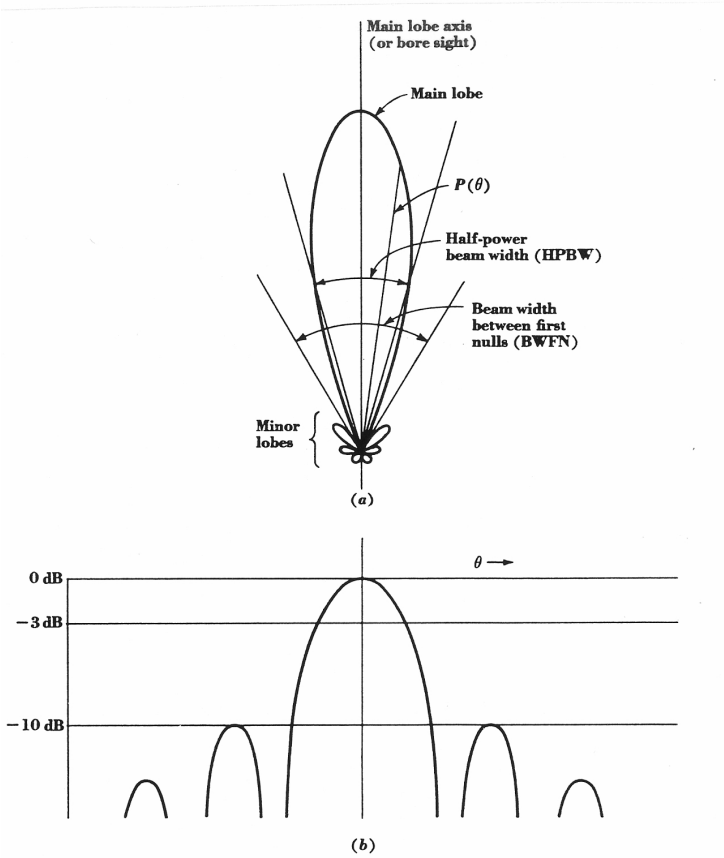

Fig. 6-1. (*a*) Antenna pattern in polar coordinates and linear power scale; (*b*) antenna pattern in rectangular coordinates and decibel power scale.

Figure 4.2: HPBW ~ BWFN/2 (beam width between first nulls). dB = 10 × log P1/P0; if P1 = P0 → 0 dB, if P1/P0 = 0.5 → 3 dB (Fig. from Kraus: Radio Astronomy)

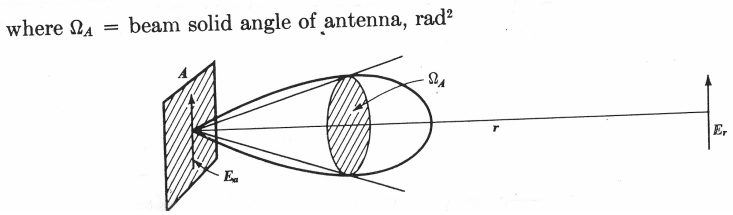

Figure 4.3: Antenna beam: The angle in **radians** (rad) is related to the arc length it cuts out: $\theta = \frac{s}{r}$, where s is arc length, and r is the radius of the circle. A squared radian is also called a **steradian** (sr), which is defined as the solid angle subtended at the center of a sphere of radius r by a portion of the surface of the sphere having an area r^2. (Fig. from Kraus: Radio Astronomy)

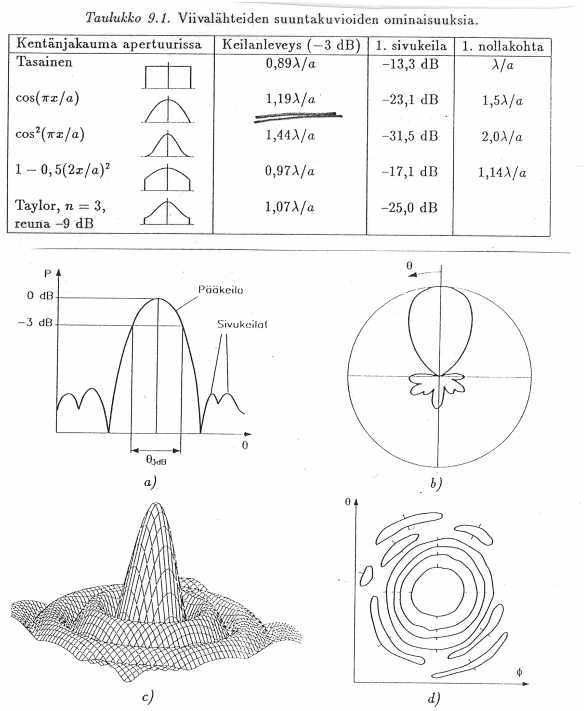

Taulukko 9.1. Viivalähteiden suuntakuvioiden ominaisuuksia.

Kentänjakauma apertuurissa	Keilanleveys (−3 dB)	1. sivukeila	1. nollakohta
Tasainen	$0{,}89\lambda/a$	−13,3 dB	λ/a
$\cos(\pi x/a)$	$1{,}19\lambda/a$	−23,1 dB	$1{,}5\lambda/a$
$\cos^2(\pi x/a)$	$1{,}44\lambda/a$	−31,5 dB	$2{,}0\lambda/a$
$1 - 0{,}5(2x/a)^2$	$0{,}97\lambda/a$	−17,1 dB	$1{,}14\lambda/a$
Taylor, $n = 3$, reuna −9 dB	$1{,}07\lambda/a$	−25,0 dB	

Kuva 9.3. *Suuntakuvion esitysmuotoja: a) suorakulmainen, b) polaarinen, c) kolmiulotteinen. d) vakioarvokäyrästö*

Figure 4.4: Spatial resolution: Antenna beamwidth – which basically means the spatial resolution – can be approximated with $\theta = 1.2\ \frac{\lambda}{D}$. (Fig. from Räisänen - Lehto: Radiotekniikka)

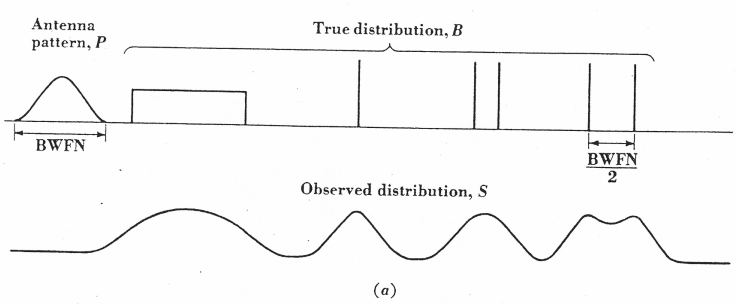

Fig. 6-11a. Smoothed distribution S observed with antenna pattern P.

(Fig. from Kraus: Radio Astronomy)

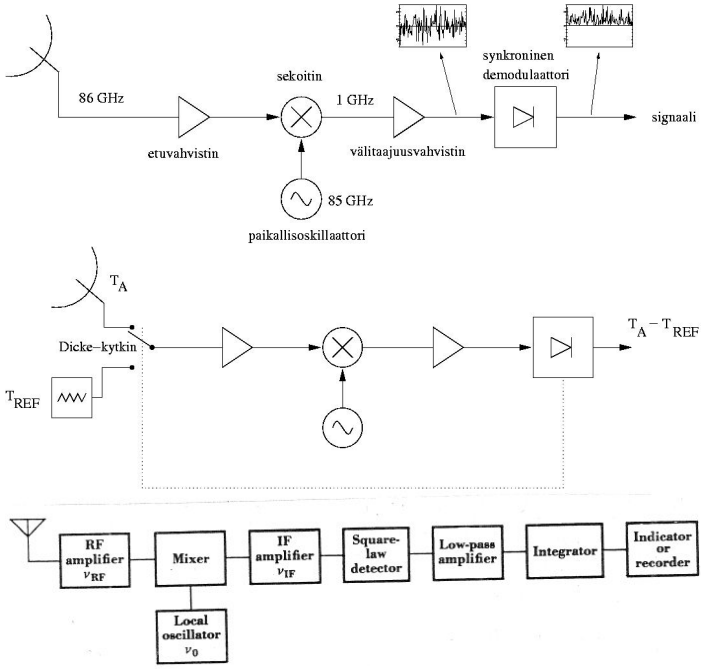

Figure 4.5: The basics of radio receivers

4.2 Interferometers

The benefit of interferometers in solar observations: better spatial resolution and removal of atmospheric disturbancies (can observe in cloudy weather). Baseline = distance between the farthermost antennas ~ D.

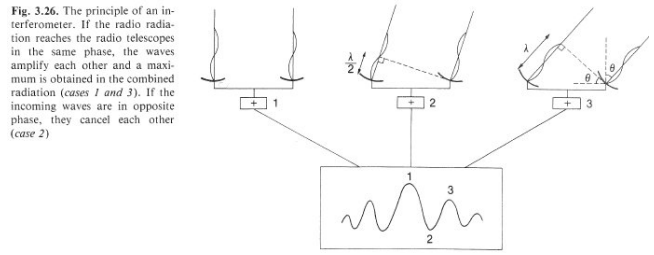

Fig. 3.26. The principle of an interferometer. If the radio radiation reaches the radio telescopes in the same phase, the waves amplify each other and a maximum is obtained in the combined radiation (*cases 1 and 3*). If the incoming waves are in opposite phase, they cancel each other (*case 2*)

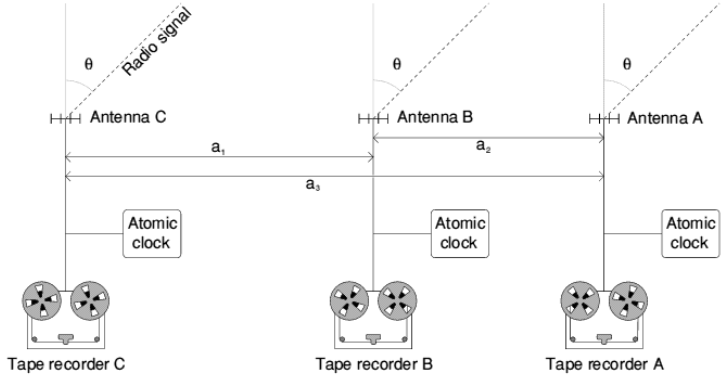

Figure 4.6: The Nobeyama radioheliograph is a traditional T-shape array of telescopes, in the future Frequency Agile Solar Radiotelescope (FASR) will consist of telescopes in no particular array form.

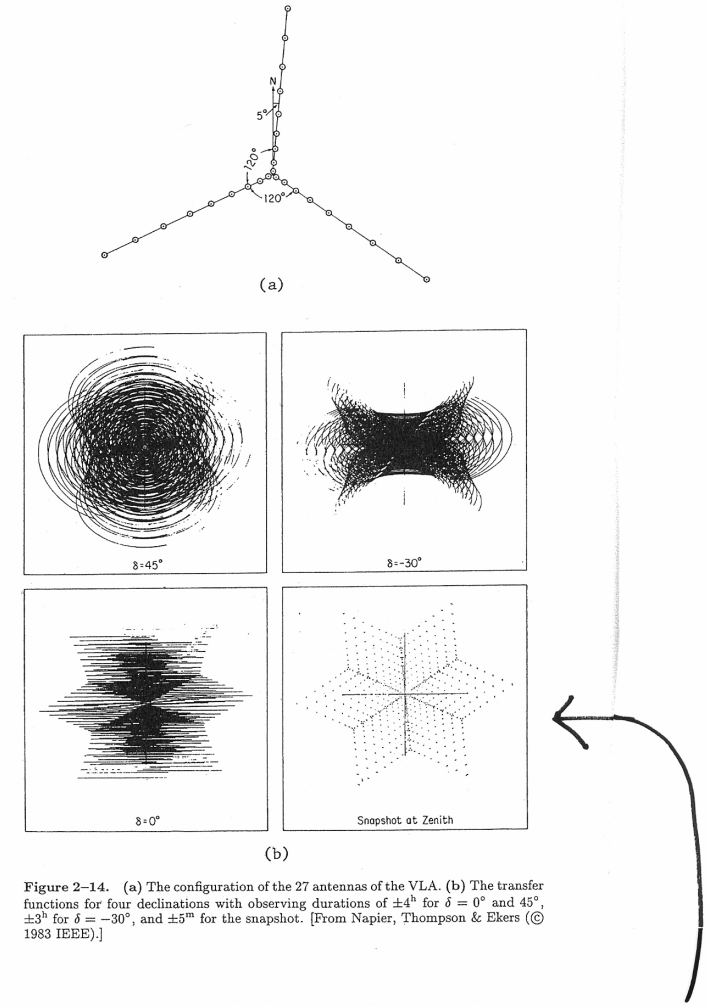

Figure 2–14. (a) The configuration of the 27 antennas of the VLA. (b) The transfer functions for four declinations with observing durations of $\pm 4^h$ for $\delta = 0°$ and 45°, $\pm 3^h$ for $\delta = -30°$, and $\pm 5^m$ for the snapshot. [From Napier, Thompson & Ekers (© 1983 IEEE).]

Figure 4.7: Solar observations are almost always done in the snapshot mode (no Earth rotation is used for the aperture synthesis).

4.3 Brightness temperature and flux density

An ideal (blackbody) radiator at temperature T radiates with intensity

$$B_\nu(T) = \frac{2h\nu^3}{c^2}\frac{1}{e^{h\nu/kT}-1} \qquad (\mathrm{W\ m^{-2}\ Hz^{-1}\ sr^{-1}}) \tag{4.1}$$

At radio frequencies we can use the Rayleigh-Jeans approximation ($e^{h\nu/kT} \sim 1 + h\nu/kT + ...$)

$$B_\nu = \frac{2kT\nu^2}{c^2} \qquad (\mathrm{W\ m^{-2}\ Hz^{-1}\ sr^{-1}}) \tag{4.2}$$

for the brightness (regardless of the emission mechanism).

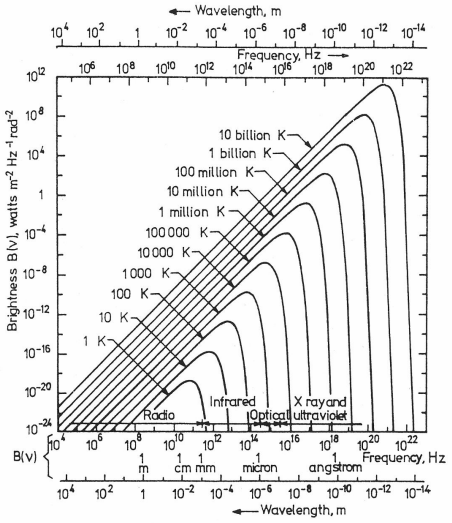

Fig. 1.6. The Planck spectrum for black bodies of different temperatures

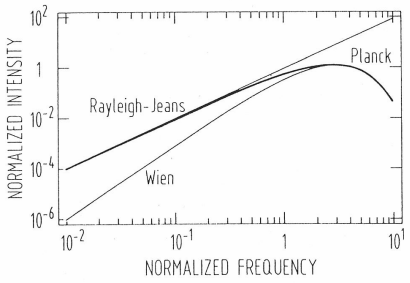

Fig. 1.7. Normalized Planck curve and the Rayleigh-Jeans and Wien approximation

Flux density S of a source is determined from the source brightness and the source solid angle

$$S = \int\int_{\Omega_S} B_S(\theta, \phi)\ d\Omega \tag{4.3}$$

If the source brightness is constant over the telescope beam area, the received power is

$$P_r = 1/2\ A_{ef}\ S_0\ \Delta f \tag{4.4}$$

where Δf is the frequency bandwidth, A_{ef} is the effective aperture of the antenna, and S_0 is the observed flux density within the antenna beam ($S_0 = B_S\ \Omega_A$).

Antenna temperature can be solved from

$$P_r = k\, T_A\, \Delta f \tag{4.5}$$

The antenna temperature T_A due to the source can be expressed as

$$T_A = \frac{1}{\Omega_A} \int\int T(\theta, \phi)\, P_n(\theta, \phi)\, d\Omega \tag{4.6}$$

$T(\theta, \phi)$ is the source temperature
$P_n(\theta, \phi)$ is the normalized antenna power pattern (dimensionless)
Ω_A is the antenna beam area (rad^2)

Flux density S of a source (for the two polarizations) is related to the source brightness temperature

$$S = \frac{2kv^2}{c^2} \int T_b\, d\Omega \qquad (\text{W m}^{-2}\ \text{Hz}^{-1}) \tag{4.7}$$

where $d\Omega$ is a differential solid angle and the integral is over the projected area of the source.

The observed flux density can then be written as

$$S_0 = \frac{2kT_A}{A_{ef}} \qquad (\text{W m}^{-2}\ \text{Hz}^{-1}) \tag{4.8}$$

Simplified Example

D= 14 m
A= πr^2 = 154 m^2
A_{ef} = 0.5 × 154 = 77 m^2
$T_A \approx T_b \approx$ 7200 K at 37 GHz (source > beam, no absorbing atmosphere)

$$S_0 = \frac{2kT_A}{A_{ef}} = 2 \times 1.3805 \times 10^{-23} \times 7200/77 \tag{4.9}$$

$$= 2.58 \times 10^{-21}\ \text{W m}^{-2}\ \text{Hz}^{-1} = 26\ \text{sfu}$$

For a 2-m antenna with similar efficiency S_0 = 1266 sfu

Example. Mayer, McCullough, and Sloanaker (1958*a*, *b*) at the Naval Research Laboratory measured an antenna temperature of 0.24 K at a wavelength of 3.15 cm, when their radio-telescope antenna was directed at Mars. At the time of the measurements the disk of Mars subtended an angle of 18 sec of arc. Assuming that the antenna has a pencil beam of 0.116° between half-power points, find the equivalent temperature of the source (Mars).

Solution. The radius of the disk of Mars is 9 sec of arc or 9/3,600 = 0.0025°. Hence, the solid angle of the disk is given by

$$\Omega_s = \pi r^2 = \pi\,(0.0025°)^2 = 2 \times 10^{-5}\ \text{deg}^2$$

The beam area Ω_A of the antenna is given approximately by (see Chap. 6)

$$\Omega_A = \tfrac{4}{3}(0.116)^2 = 0.018\ \text{deg}^2$$

Hence, assuming a constant temperature over the disk, the average equivalent temperature of Mars by this measurement is, from (3-118),

$$T = T_A \frac{\Omega_A}{\Omega_s} = 0.24\,\frac{0.018}{2 \times 10^{-5}} = 216°$$

(from Kraus: Radio Astronomy)

If the source size (Ω_s) is smaller than the antenna beam size (Ω_A), the observed antenna temperature reduces to:

$$T_A = \frac{\Omega_s}{\Omega_A}\,T_b \tag{4.10}$$

Relative radio flare brightness:

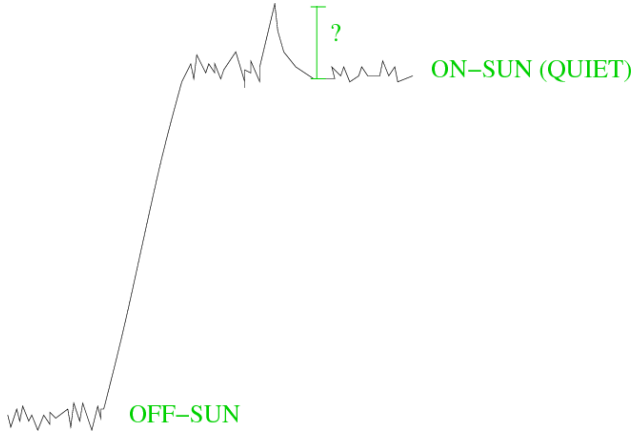

$T_{b,\nu}$ = X Kelvin (quiet Sun brightness temperature at frequency ν from literature or absolute calibrations)
On-Sun − Off-Sun = Y mV

⇒ Y mV ≡ X Kelvin

Calibration

- Absolute calibration using radio sources and hot+cold loads
- No calibration, using units relative to 'quiet Sun' level

The method of using relative solar flux units provides the advantage of removing atmospheric and radome effects (variable attenuation) and instrumental effects, but it is more sensitive to errors in quiet Sun level determination.

Furthermore, the true source size of the radio emitting region in solar flares is not always known and it can vary from a few arc seconds to several arc minutes.

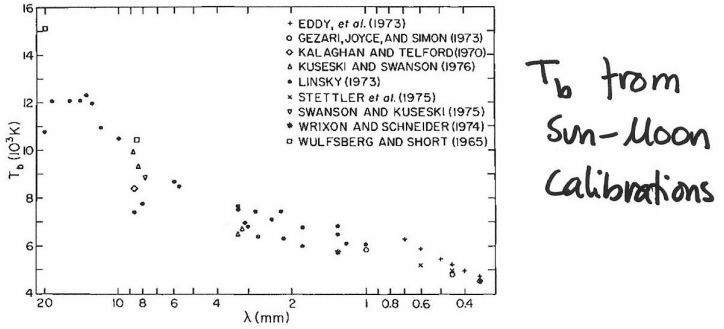

T_b from Sun–Moon Calibrations

FIG. 5.—Selected brightness temperature observations of the Sun at millimeter wavelengths

Figure 4.8: (Vernazza, Avrett & Loeser, 1981)

Sensitivity

The sensitivity of radio observations depends on the receiver noise temperature, i.e. the receiver must be able to detect small differences in the total noise. The sensitivity of the system is calculated from the total or system noise temperature T_{sys}

$$T_{sys} = T_A + T_R \tag{4.11}$$

where T_R is the receiver noise temperature (K). The smaller the antenna (source) temperature, the smaller should the receiver noise temperature be.

In some cases the sensitivity limitation can be overcome by longer integration time or larger bandwidth.

The minimum detectable temperature ΔT of a radio telescope is

$$\Delta T = \frac{K_s\, T_{sys}}{\sqrt{\Delta f\, t}} \tag{4.12}$$

where K_s is a sensitivity constant that depends on the receiver type, Δf is the receiver bandwidth (Hz) and t is the post-detection integration time (s).

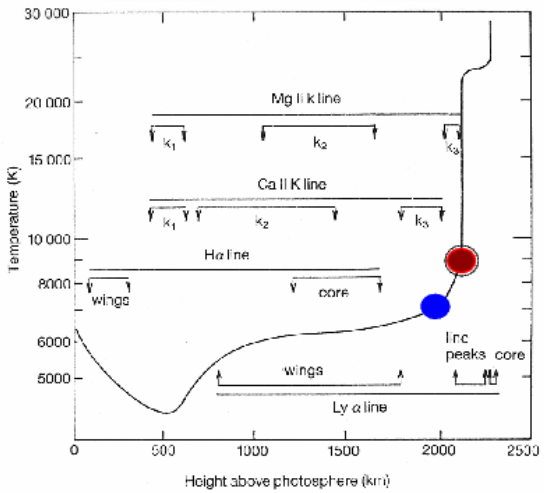

Fig. 4.12 The variation of temperature with height in the solar atmosphere up to the transition region for an average quiet-sun region. Also indicated are the height ranges over which the Hα and Ly-α, Ca II H and K, and Mg II h and k lines are formed. (After Vernazza, Avrett and Loeser (1981))

13 mm radio emission (quiet Sun, plasma limit)

3 mm radio emission (quiet Sun, plasma limit)

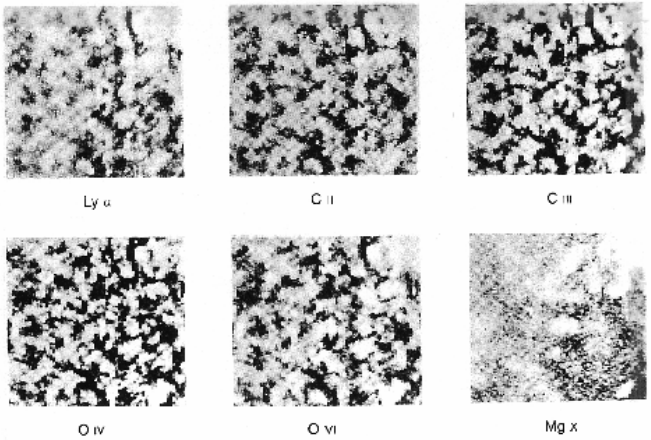

Fig. 4.11 Six *Skylab* images of a quiet-sun region taken in ultraviolet spectral lines in a temperature range from the chromospheric Lyman-α to the coronal Mg X. The chromospheric network becomes progressively more blurred. (Courtesy R. Noyes, Harvard College Observatory and NASA)

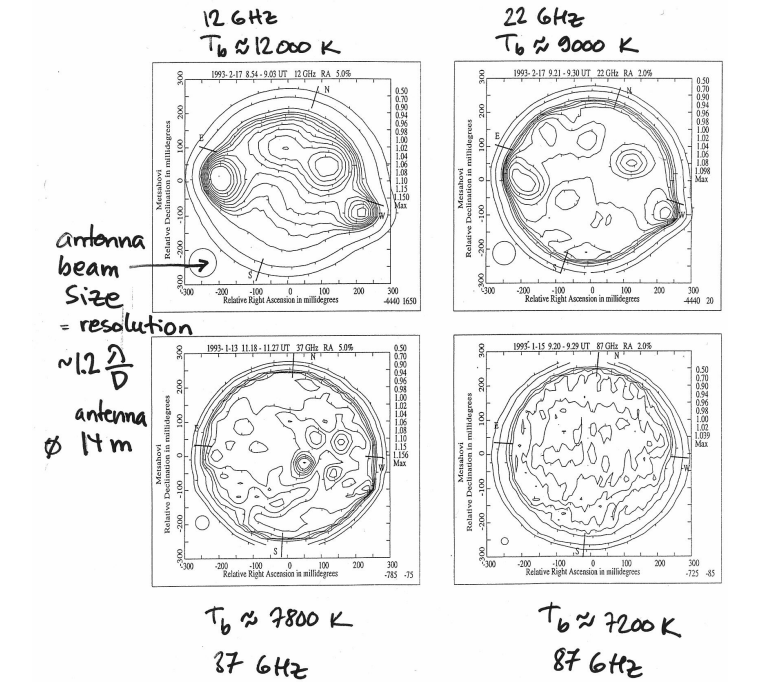

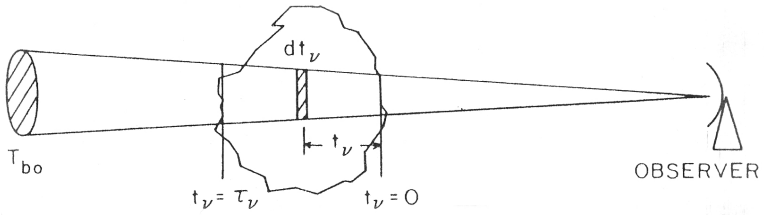

4.4 Radiative transfer equations

Geometry of a source with effective temperature T_{eff} and optical depth τ, located in front of a background with brightness temperature T_{bo}.

$$T_b = \int_0^{\tau_\nu} T_{eff} e^{-t_\nu} dt_\nu + T_{bo} e^{-\tau_\nu} = T_{eff}(1 - e^{-t_\nu}) + T_{bo} e^{-\tau_\nu} \tag{4.13}$$

Just the source, with no background:

$$T_b = \int_0^{\tau_\nu} T_{eff} e^{-t_\nu} dt_\nu \tag{4.14}$$

$$T_b = T_{eff}(1 - e^{-t_\nu}) \tag{4.15}$$

if $\tau_\nu \gg 1$, $e^{-t_\nu} \to 0$: $T_b = T_{eff}$ (optically thick)

if $\tau_\nu \ll 1$, $(1 - e^{-t_\nu}) \to \tau_\nu$: $T_b = T_{eff}\,\tau_\nu$ (optically thin).

Example:

An emission source, with brightness temperature of 200 K and source solid angle of 1 deg^2 is observed through a cloud. The brightness temperature of the cloud is 100 K and its solid angle is 5 deg^2. The effective area of the radio telescope is 50 m^2. Observations are done at 600 MHz and the optical depth of the cloud is 1. Calculate the antenna temperature when the telescope is pointing to the source (you can ignore the 3 K cosmic background radiation).

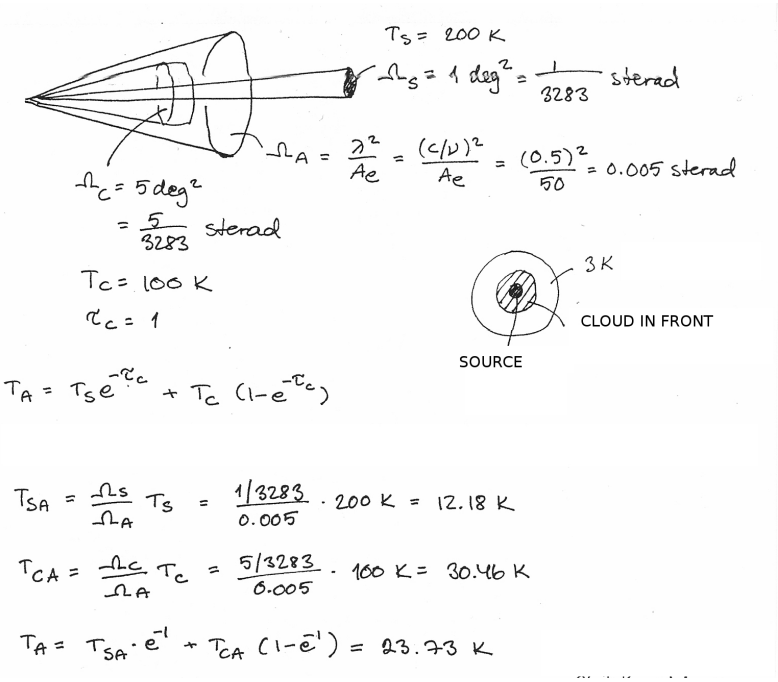

Bremsstrahlung emissivity

$$\varepsilon_\nu = \frac{8}{3}\left(\frac{2\pi}{3}\right)^{1/2}\frac{z^2e^6}{m^2c^2}\left(\frac{m}{kT}\right)^{1/2} N_i N_e\, g(\nu,T)\, e^{-h\nu/kT}$$

$$= 5.4\cdot10^{-39}\frac{N^2}{T^{1/2}}\, e^{-h\nu/kT}\, g(\nu,T) \quad \text{erg/s cm}^3\,\text{Hz rad}$$

radio $h\nu \ll kT \Rightarrow e^{-h\nu/kT} \approx 1$

$$\Rightarrow \varepsilon_\nu(\text{radio}) = 5.4\times10^{-39}\frac{N^2}{T^{1/2}}\, g(\nu,T)$$

For $T > 3.6\cdot10^5$ K, $g(\nu,T) \simeq \frac{\sqrt{3}}{\pi}\ln\left(\frac{4kT}{h\nu}\right)$

$$\simeq (24.5 + \ln T - \ln\nu)\frac{\sqrt{3}}{\pi}$$

$$\Rightarrow \varepsilon_\nu(\text{radio}) = 2.98\cdot10^{-39}\frac{(24.5+\ln T-\ln\nu)}{T^{1/2}}N^2$$

Brightness

$$\Rightarrow I_\nu = \int \varepsilon_\nu\, ds = 2.98\cdot10^{-39}\frac{(24.5+\ln T-\ln\nu)}{T^{1/2}}\cdot EM$$

$(EM = \int N^2\, ds)$

Flux density

$$S = \int I_\nu\, d\Omega = I_\nu\left(\frac{L}{D}\right)^2$$

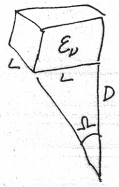

$D = 1.5\cdot10^{13}$ cm

$$\begin{pmatrix}\text{radio:} & EM = \int N^2\, dL = \bar{N}^2 L \\ \text{x-ray:} & EM = \int N^2\, dV = \bar{N}^2 L^3\end{pmatrix}$$

$$\Rightarrow S_{\text{radio}} = \varepsilon_\nu \cdot L\cdot\left(\frac{L}{D}\right)^2 = \frac{\varepsilon_\nu L^3}{D^2} = \frac{2.98\cdot10^{-39} f(T,\nu)\cdot EM_{\text{x-ray}}}{D^2}$$

$$= 1.32\cdot10^{-65} f(T,\nu)\cdot EM_{\text{x-ray}}, \quad \text{erg/cm}^2\,\text{Hz}$$

$$= 1.32\cdot10^{-68} f(T,\nu)\, EM_{\text{x-ray}}, \quad \text{W/m}^2\,\text{Hz}$$

$$= 1.32\cdot10^{-46}\left(\frac{24.5+\ln T-\ln\nu}{T^{1/2}}\right) EM_{\text{x-ray}}, \quad \text{stu}$$

4.5 Radio observations

- Large single dish antennas (Metsähovi and Itapetinga 14 m, Nobeyama 45 m)
- Small dish complexes (Bern/Tuorla, Nobeyama polarimeters NoRP)
- Non-traditional antennas (RATAN-600)
- Multi-beam receivers in single dish (Brazil, Argentina)
- Interferometers (Nancay radioheliograph NRH, Nobeyama radioheliograph NoRH, Owens Valley Solar Array OVSA, future FASR)
- Radio spectrografs (Zurich ETHZ, Tremsdorf OSRA, Artemis-IV in Greece, HiRAS in Japan, Culgoora in Australia, etc.)
- Radio spectrometers in space (Wind WAVES and STEREO WAVES)
- Solar eclipse observations

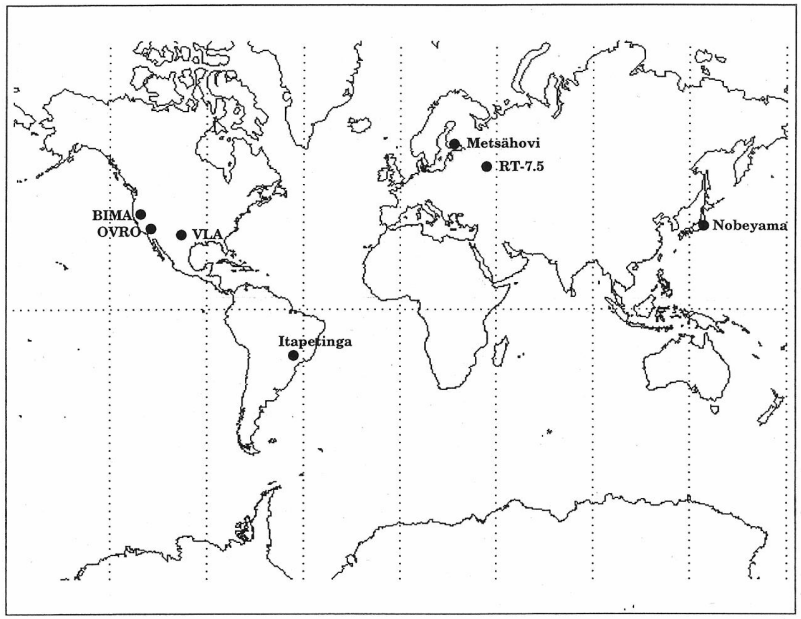

Figure 4.9: Radio facilities at cm- and mm-wavelengths (note the time difference, limited common observing time).

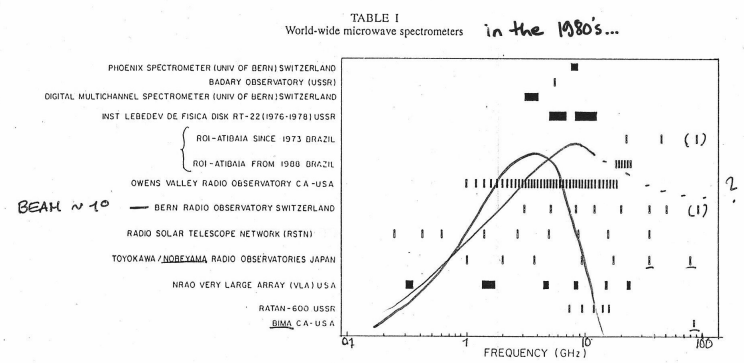

Figure 4.10: Fixed frequency coverage in the 1980s..

4.5.1 Single dish antennas

Figure 4.11: Single dish antennas - Metsähovi Radio Observatory, a 14-m antenna in Kirkkonummi, operated by Helsinki University of Technology

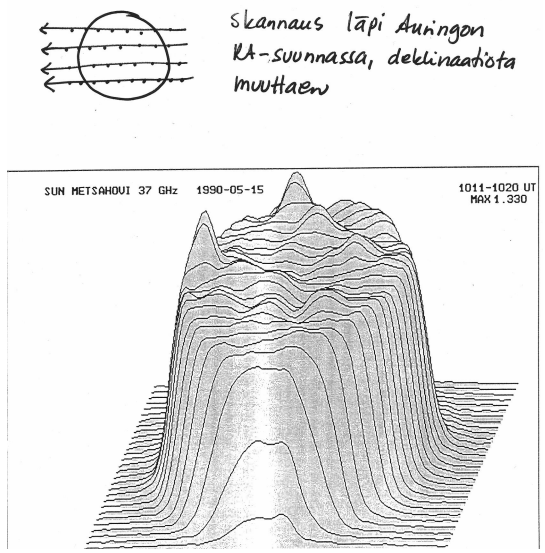

Figure 4.12: Imaging with scanning technique, the scans are made along right ascension, changing declination between scans.

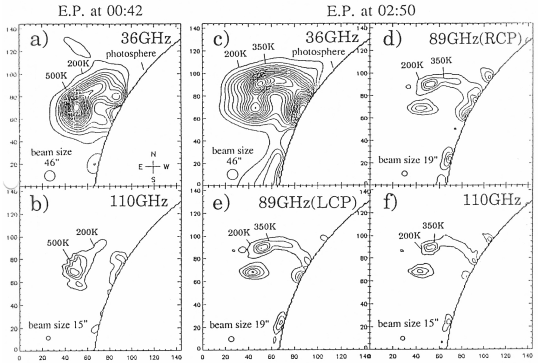

Fig. 1. Contour maps of the eruptive prominence at millimeter wavelengths observed with the 45-m radio telescope at Nobeyama Radio Observatory. (a) and (b) show 'E.P. at 00:42' observed from 00:42 to 00:55 UT (May 28) at 36 and 110 GHz, respectively. The minimum contour level is 200 K. The contour step is 300 K. (c–f) show 'E.P. at 02:50' observed from 02:50 to 02:59 UT (May 28) at 36 GHz, 89 GHz (RCP), 89 GHz (LCP), and 110 GHz, respectively. The minimum contour level is 200 K and the contour step is 150 K. The unit for each axis is 5″. The area of the maps is 12′ × 12′, and the spatial resolutions are 46″, 19″, and 15″ at 36, 89, and 110 GHz, respectively. The heights of the prominence are about 1.5×10^5 km and 1.7×10^5 km above the photosphere for 'E.P. at 00:42' and 'E.P. at 02:50', respectively.

Figure 4.13: Nobeyama 45-m scanning observations of a prominence (full disk needs 240 scans, which is done in 2 hours time!) From Irimajiri et al. 1995

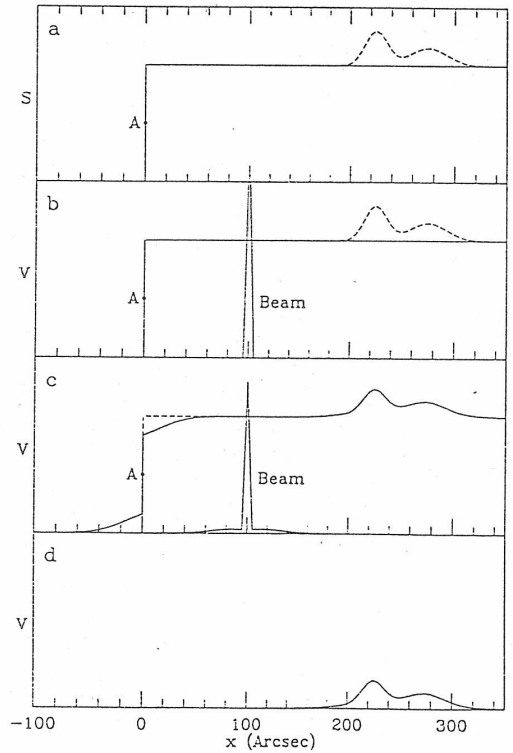

FIG. 3.—Diagrams illustrating the result of convolving sources with beams that have a sharp core and symmetric far wings. (*a*) Shows a source consisting of a simple step-function discontinuity (*solid curve*) at x (i.e., a Heaviside function). The dashed curve shows continuous variations introduced well inside the discontinuity. (*b*) Shows the result, V, of convolving the source in (*a*) with a simple Dirac delta function with no wings, which duplicates the source exactly. (*c*) Illustrates artificial limb darkening with an equal measure of artificial sky brightening, which results when the source profile is convolved with a beam that has symmetric wings. (*d*) Shows only continuous variation far to the right without the limb discontinuity. If we are given that the far wings of the beam are symmetric, we can conclude that the signal profiles in (*b*) and (*c*) can only have come from the source plotted in (*a*). The source that gave rise to the smooth signal profile shown in (*d*) remains ambiguous without further knowledge of the beam profile.

Figure 4.14: Artificial limb darkening (Lindsey and Roellig)

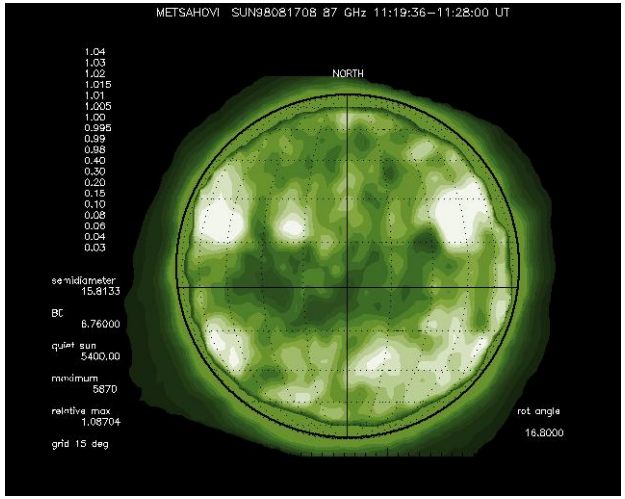

Figure 4.15: Artificial limb darkening observed in a Metsähovi solar map.

Figure 4.16: Small dish complexes: Tuorla-Bern polarimeters (TUBE)

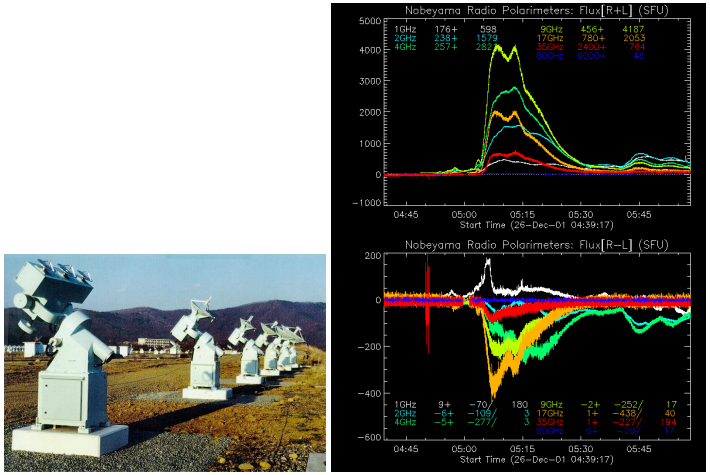

Figure 4.17: Nobeyama polarimeters: Fixed frequencies at 1, 2, 3.75, 9.4, 17, 35, 80 GHz, full disk observations, automatic recording

4.5.2 Non-traditional antennas

RATAN 600 (Russia)
RATAN 600 consists of 895 antenna elements (2×11.5 m each), constructed in the shape of a ring with a diameter of 576 m. One-dimensional scans of the Sun are observed near 09 UT, at 30-40 wavelengths ranging from 1.67 cm up to 32 cm with left (LCP) and right (RCP) circular polarization.

Figure 4.18: RATAN-600 in Zelenchukskaya, North Caucasus, Russia

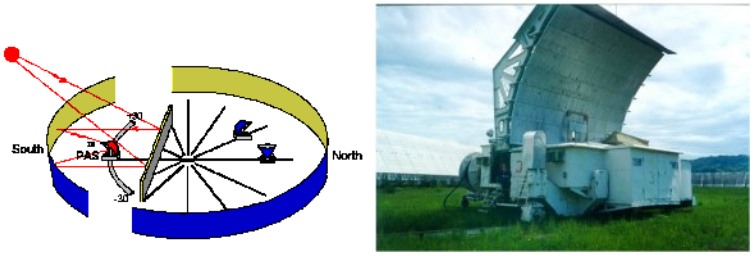

Figure 4.19: The RATAN-600 is a reflector-type radio telescope, advantages being a broad wavelength range, ability to use wide bandwidths, etc., but it is non-traditional in design. In order to obtain high resolution at rather short wavelengths, the mirror of a radio telescope must have rather large linear dimensions and the reflecting surface must be extremely accurate. These requirements are clearly contradictory; in order to resolve this contradiction, the main mirror of the telescope was built in the shape of a ring. Left: the southern sector can operate in combination with the flat periscope reflector. It is possible to track a source by moving the secondary mirror along the arc-shaped railway tracks or to perform azimuthal 2D map synthesis. Right: the secondary mirror and receiver cabins.

4.5.3 Observed polarization

Stokes parameters
Stokes parameters (I,Q,U,V) describe the degree of polarization. In solar radiation only circular polarization is observed (linear polarization disappears because of Faraday rotation).

For a completely polarized wave:
Left-hand circular ('L'): I=S, Q=0, U=0, V=S
Right-hand circular ('R'): I=S, Q=0, U=0, V= –S
Note: for engineers and physicists the directions are different!

Flux density S is often described with intensity I = R+L and polarization with R-L.

Degree of polarization = polarized power/total power = $\frac{\sqrt{Q^2+U^2+V^2}}{I}$; (0...1)

Measurement of magnetic fields
In the presence of a temperature gradient, free-free radiation becomes circularly polarized:

$P = (n\,\nu_B\,\cos\alpha)/f$,

$n = -(\partial T_B/\partial f)\,f\,T_B^{-1} = \frac{\partial lgT_B}{\partial lgf}$,

where
P is the observed circular polarization degree (per cent, %),
n is the logarithmic spectral index,
ν_B is the gyrofrequency and f is the observing frequency,
T_B is the brightness temperature.

The intensity of polarized emission is proportional to the longitudinal (line-of-sight) component of the magnetic field B ($\cos\alpha = 1$).

A practical estimate is: $B = 107\,P\,(n\lambda)^{-1}$, B in Gauss and λ in cm.

For optically thin plasma, $n = 2$, and $B = 54\ P / \lambda$.

See details in e.g., Grebinskij et al., Astronomy and Astrophysics Supplement Series Vol. 144, pp. 169-180, 2000, and/or
Bogod and Gelfreikh, Solar Physics Vol. 67, pp. 29-46, 1980.

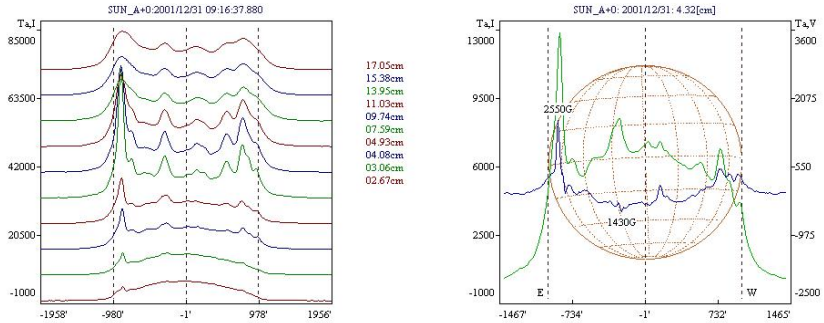

Figure 4.20: RATAN intensity profiles over the solar disk; Calculated magnetic field strength from observed polarization.

Faraday rotation

Faraday rotation observations are unique among remote diagnostics of the solar corona in that they provide information on the coronal magnetic field. The polarized radiation from natural radio sources (i.e., linear polarization of sources like quasars that get occulted by the solar corona) are observed and the magnitudes of the rotation measures together with the estimated electron number densities are used for determining the magnetic field strengths ($\beta = C \times N\, B\, \lambda^2\, \Delta d$).
See more details in Mancuso and Spangler, Astrophysical Journal, Vol 539, pp. 480-491.

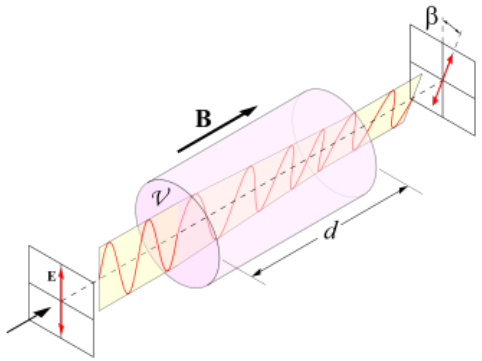

Figure 4.21: Faraday effect (image: Wikimedia Commons)

4.5.4 Multi-beam receivers in single dishes

Figure 4.22: El Leoncito, Argentina (at height 2550 m)

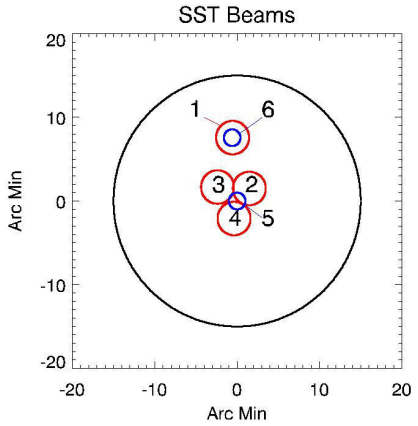

Figure 4.23: A cluster of six beams, shown in the diagram, is directed to the active region selected for tracking. Observing frequencies are 212 and 405 GHz.

A&A, 317,232, 1997

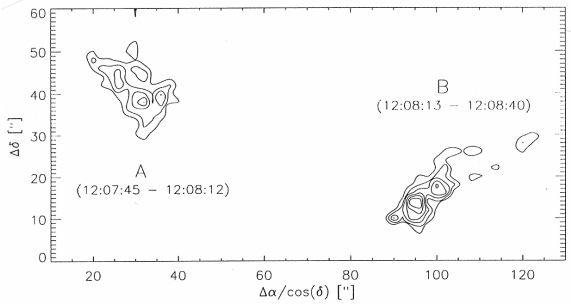

Fig. 8. Dynamic burst map of the emission center distribution during the whole event. The grid spacing is 2" and approx. 17000 positions each one calculated within 4 ms during the time interval from 12:07:45 UT until 12:08:50 UT have been used. Before 12:08:12.5 UT emission from source A dominates while for later times source B is dominant. Coordinates refer to offsets in right ascension and declination relative to the antenna pointing.

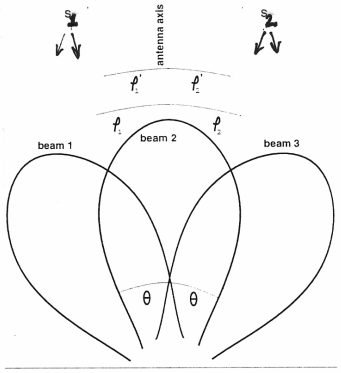

Fig. 1. Sketch of a simple antenna beam pattern of three intersecting beams observing two sources that emit at the same time.

4.5.5 Interferometers

Nobeyama Radioheliograph (NoRH) in Japan is a radio telescope dedicated to observe the Sun. "Helio" means the Sun, "graph" means an imaging telescope. It consists of 84 parabolic antennas with 80 cm diameter, sitting on lines of 490 m long in the east/west and of 220 m long in the north/south. Its construction took 2 years and cost 1.8 billion yen. The first observation was in April, 1992 and the daily 8-hours observation has been done since June, 1992. The observiong frequencies are 17GHz (right and left circular polarization) and 34GHz (only intensity). Field of view is full solar disk, with spatial resolution of 10 arcsec (17GHz) and 5 arcsec (34GHz). Temporal resolution is 0.1 sec (event mode) or 1 sec (regular mode).

As the NoRH is a radio interferometer, original data are sets of correlation values of all the combination of antennas. They correspond to the spatial Fourier components of the brightness distribution of the solar disk. In most cases, it is necessary to synthesize images from the original raw data.

NoRH image synthesis is done with IDL software. All computers use Linux as the operating system. The synthesis programs available are:

- Hanaoka (standard CLEAN algorithm, support 17 and 34 GHz, full/partial Sun images)
- Koshix (CLEAN + Steer algorithm, support 17 GHz, better for diffuse radio sources, full/partial Sun)
- Fujiki (high spatial resolution, support 17 GHz, only partial Sun images)
- C2FITS (for reconstructing the NoRH raw data to visibility data that can be utilized for AIPS synthesizing software)

Nancay radioheliograph (NRH) in France consists of a cross-shaped multi-antenna array, comprising an East-West branch with 19 antennas along a 3200 meter long baseline and a North-South branch of 24 antennas over a total length of 1250 meters. It can image the Sun at wavelengths between 60 cm and 2 meters. It has been equiped with a digital correlator, which permits the true two-dimensional imaging of the solar corona, using all possible baselines of the cross-shaped array, at a rate of 5 images per second in each of 5 fixed wavelengths between 60 cm and 2 meters. Observations at different wavelengths probe different heights in the corona, in the case of the Nancay radioheliograph regions between 0.1 and 0.5 solar radius above the visible surface.

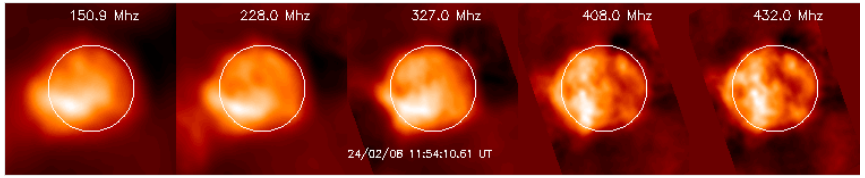

Figure 4.24: Nancay radioheliograph imaging at five selected frequencies

It is an instrument dedicated to solar observations, and presently it is the only instrument to provide daily radio observations of the **solar corona** (the other dedicated solar radio telescope, at Nobeyama Radio Observatory in Japan, observes at much shorter, centrimetric, wavelengths which probe the solar atmosphere much closer to the visible surface, and other radio telescopes, like the Very Large Array (VLA) in the U.S.A., observe the Sun only infrequently, and have not been designed for such specialized observations of a highly variable, very intense radio source).

During 1994-1998 the system has been renovated: a new, powerful correlator allowing rapid multifrequency two-dimensional imaging of the Sun has been installed, and a new 7.5 meter diameter antenna is raised at a site 1.5 km to the South of the southernmost existing antenna, thus allowing a twice better resolution. This renovation cost somewhat over a million US dollars, co-financed by the French State (CNRS) and the administrative council of the Region to which Nancay belongs.

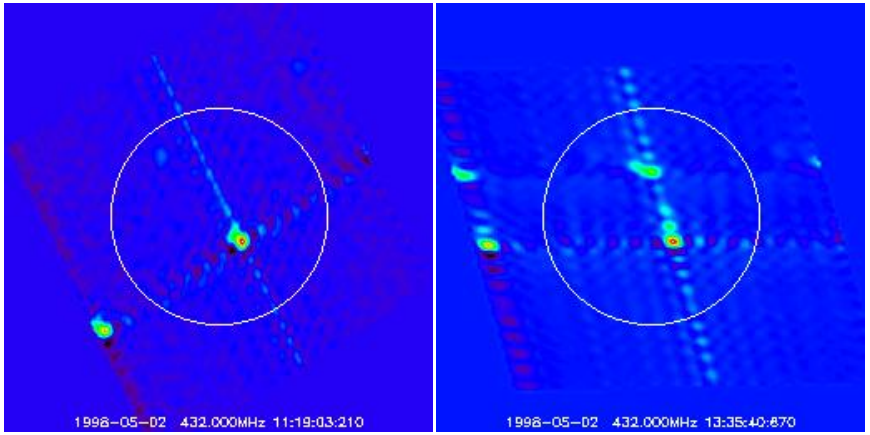

Figure 4.25: Nancay interferometric pattern + uncleaned source at 432 MHz

Interferometers - Owens Valley Solar Array (OVSA):
2 x 27-m + 3 x 2-m + 2 new 2-m antennas
1-18 GHz (tunable, phase lock in 20 ms)

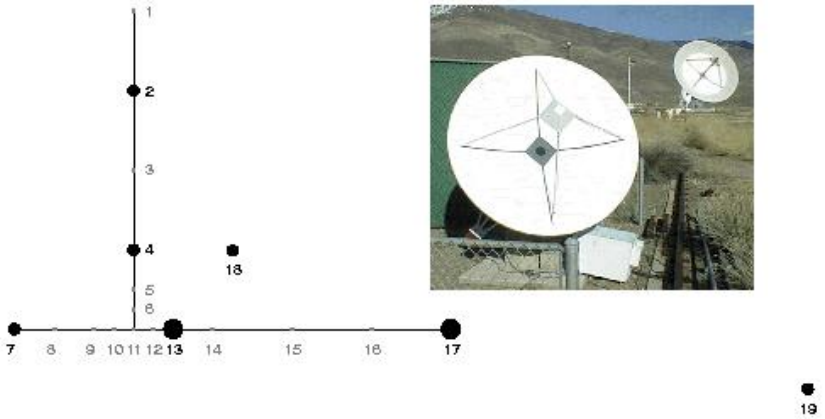

Figure 4.26: Owens Valley Solar Array (OVSA), USA

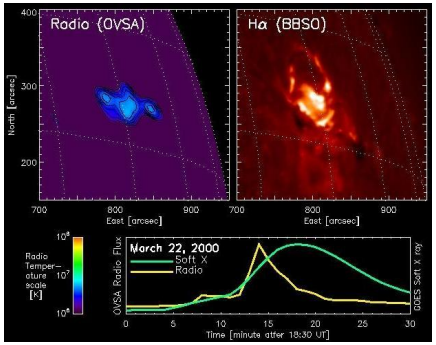

Figure 4.27: Owens Valley Solar Array (OVSA) flare observations, partial field-of-view

Figure 4.28: VLA, Socorro New Mexico, recently upgraded as Karl G. Jansky Very Large Array, with state-of-art receivers and electronics, enabling dynamic imaging spectroscopic observations of the Sun.

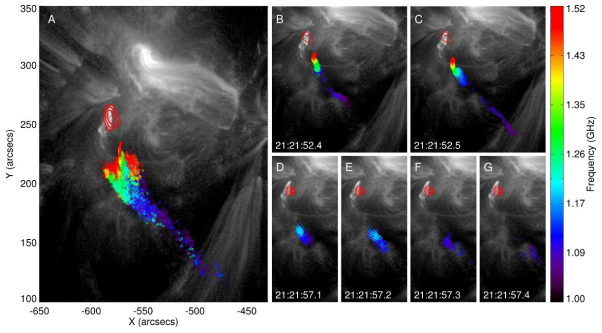

Figure 4.29: Type IIIdm burst centroids as a function of frequency (colored from red to blue for decreasing frequencies), showing trajectories of fast electron beams in the solar corona. See RHESSI Science Nugget at http://sprg.ssl.berkeley.edu/~tohban/wiki/index.php/Passages_of_Electron_Beams

4.5.6 Radio spectrometers

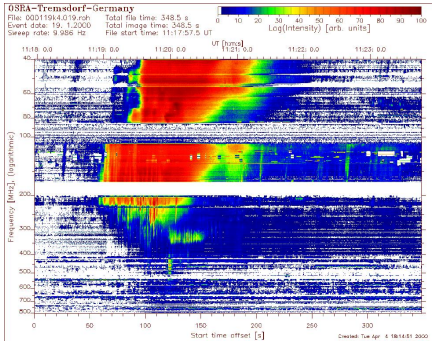

Figure 4.30: Note the missing frequencies, removed because of man-made interferences.

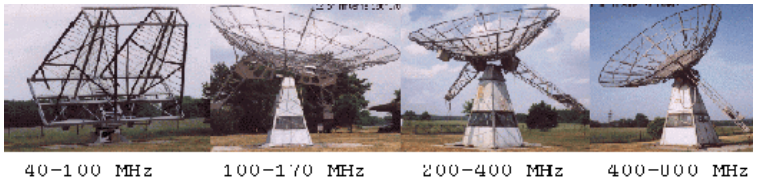

Figure 4.31: Examples of radio spectrometers: Tremsdorf in Germany. The systems consists of 4 sweep spectrographs (10 sweeps per second): 40-90 Mz, 100-170 MHz, 200-400 MHz, 400-800 MHz. The antennas are a pair of crossed double-log Yagis, 1 x 10.5-m, 2 x 7.5-m paraboloids. There is strong interference at 85-108 MHz (UHF radio), 170-200 MHz (UHF TV), 550-700 MHz (VHF TV). Calibration between frequency ranges can also be tricky.

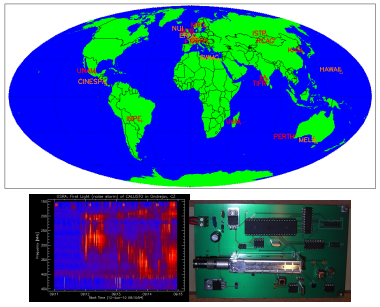

Figure 4.32: New cheap and smart technology: e-Callisto (operated by Christian Monstein, ETH Zurich)

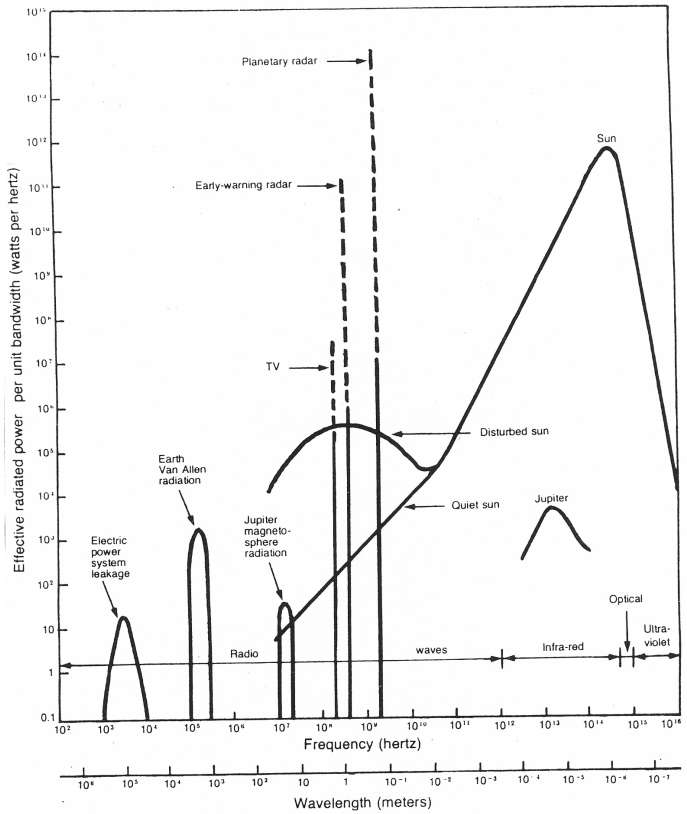

Fig. 8-51. Electromagnetic spectrum of the solar system from radio to UV showing the spectral power (W Hz^{-1}) as a function of frequency for sources of radiation from the earth, Jupiter and the sun. The largest spectral powers are from terrestrial radars.

Figure 4.33: Interferences may appear at IF, not just at observing frequencies. (Fig. from Kraus: Radio Astronomy)

The plasma frequency of the ionosphere is ~15 MHz on the day side of the earth near sunspot maximum and ~10 MHz on the night side near sunspot minimum, making the layer opaque to all lower frequencies. Even at preferred sites near the magnetic poles, such as Canada and Tasmania, and near sunspot minimum when ground based observations can be taken as low as 2~ MHz, the available resolution is extremely poor (several degrees). Therefore, to study this last unexplored window on the electromagnetic universe, one must go to space.

The Wind **WAVES** investigation (launched in 1994), with two swept-frequency radio receivers RAD1 and RAD2, provides comprehensive coverage of radio and plasma wave phenomena in the frequency range from 20 kHz up to about 14 MHz. The Thermal Noise Receiver TNR extends the frequency range down to 4 kHz. STEREO (launched in 2006) and Solar Orbiter (to be launched around 2015) will provide similar radio spectral data.

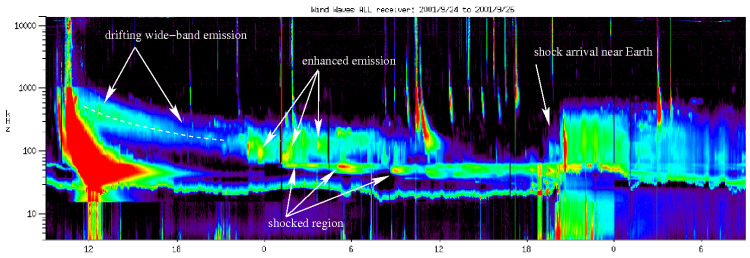

Figure 4.34: Radio spectrometers in space - Wind WAVES example.

4.5.7 Solar eclipse observations using Fresnel diffraction

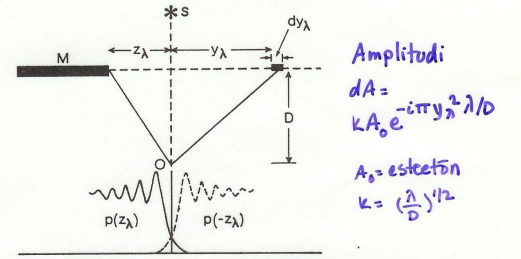

FIG. 1. Schematic representation of the generation of the occultation curve $p(z_\lambda)$, as the screen M at a distance D from the observer uncovers a source S. The occultation curve is the mirror image about the axis OS of the diffraction curve $p(-z_\lambda)$.

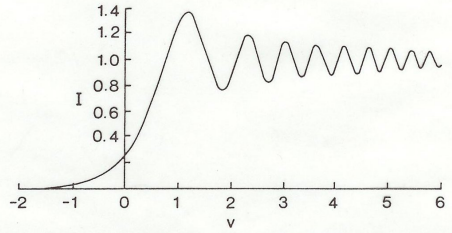

FIG. 2. The shape of the occultation curve of a point source. The horizontal scale is in units of v, the corresponding angular scale being given by $\theta = v(\lambda/2D)^{1/2}$, where λ is the wavelength and D the Moon's distance. For $\lambda = 1$ m, one unit of v corresponds to about 8 arc sec. $I = 1$ corresponds to the flux density of the unobstructed curve, while at the edge of the geometrical shadow $I = 0.25$.

Hazard, 1976

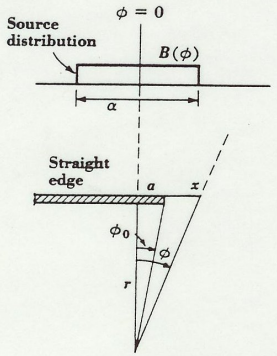

Kohteen nopeus diffraktiokuvion yli (kohtisuoraan kuun reunaa vastaan)

Aika t / 1"

$$t = \frac{1}{\frac{d\theta}{dt}\cos\theta}$$

$\frac{d\theta}{dt}$ = kuun etenemisnopeus arc sec/s $\approx 0.''3/s$

θ = kuun etenemissuunnan ja kohteen välinen kulma

Fig. 6-35. Occultation of source of width α.

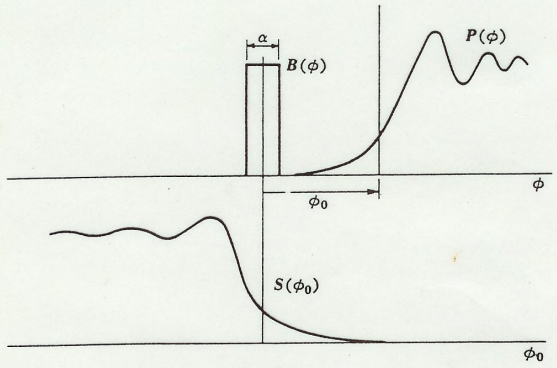

Fig. 6-36. The occultation curve is the convolution of the source distribution and the occultation pattern for a point source.

$$S(\phi_0) = \int_{-\alpha/2}^{+\alpha/2} B(\phi)\tilde{P}(\phi_0 - \phi)\, d\phi$$

Kraus, 1986

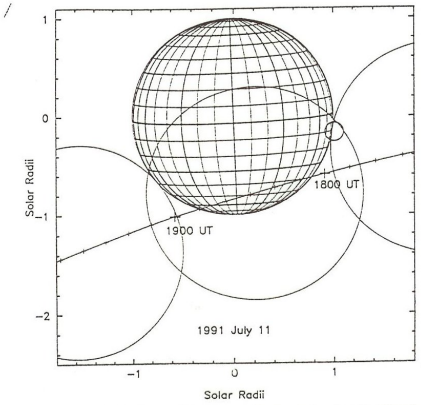

FIG. 1.—Path of the Moon with respect to the Sun during the eclipse (north is at the top of the figure and west to the right). The relative size of the main beam is shown by a circle. The interferometer tracked a point 10″ above the photospheric limb.

Kuun liike 0.4″/s
integrointiaika 8.2 s
resoluutio 1″3

20 s × 0.4″ ≈ 8″

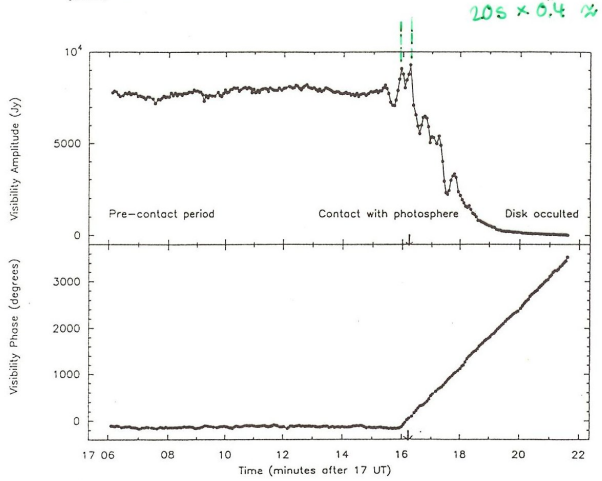

FIG. 2.—Amplitude (*top panel*) and phase (*bottom panel*) of the visibility around the time of first contact, for a baseline with fringes parallel to the limbs. The behavior of each is explained in the text. The arrows point to the time at which the photosphere was occulted.

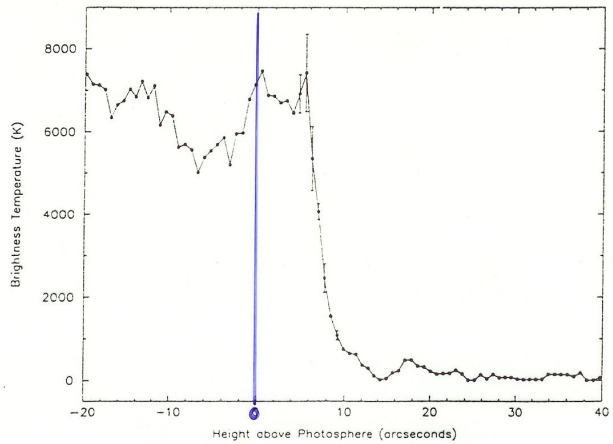

FIG. 5.—The limb profile, derived using the ephemeris phases. The attenuation due to the primary beam has been removed.

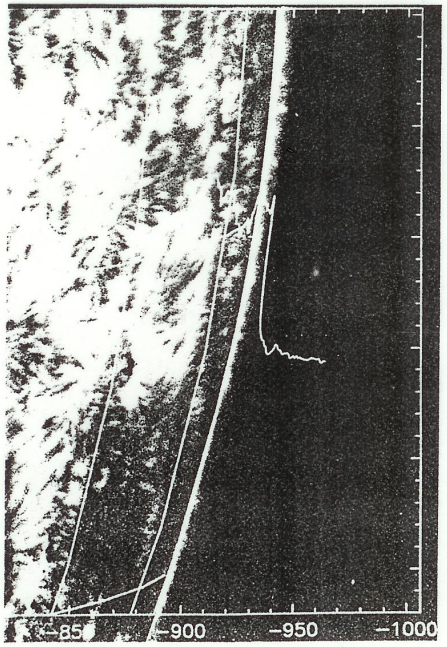

FIG. 6.—Off-band Hα photograph of the region near the limb, taken at BBSO on the day of the eclipse, overlaid with solar latitude and longitude lines at 10° intervals and with a plot of the 3 mm limb profile. *The vertical scale of the radio profile is arbitrary.* The plus sign shows the center of the beam. The spicules can be seen as a fuzzy edge above the optical limb, nearly at the same height as the sharp cutoff in the radio profile. The contrast of the Hα spicules was photographically enhanced for clarity.

Bellcore,... 1992.

4.5.8 Burst classifications

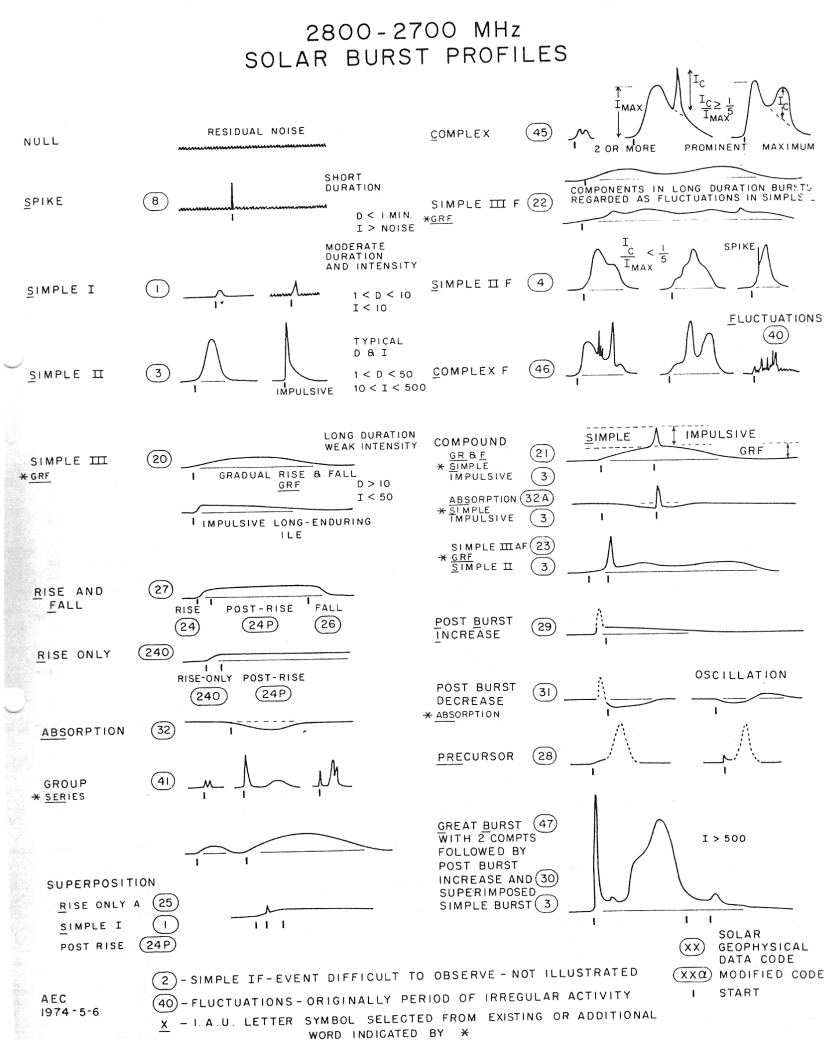

Solar burst classification using radio emission at 2.8 GHz. Many flare forecasts are done using this wavelength
F10.7 = 2800 MHz = 10.7 cm flux

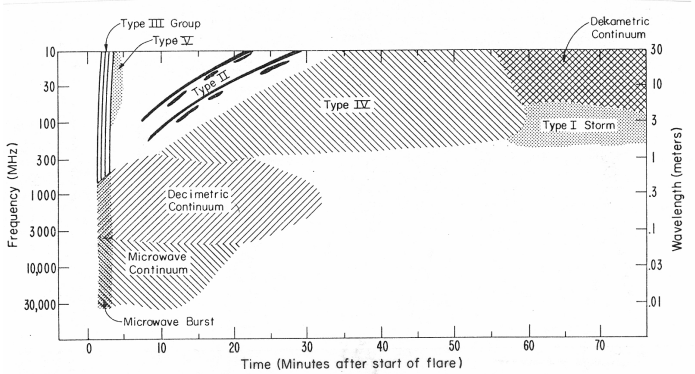

Spectral type --

I = storm bursts
II = slow drift bursts
III = fast drift bursts
IV = prolonged continuum
V = brief continuum (normally following Type III burst)

CONTINUUM = continuum in close association with Type III burst storms, often with reverse drift bursts and often, but not always, associated with noise storms on metric wavelengths (used by SMGR);
DCIM = decimetric burst defined by very fast drift spike or group of spikes with very high degree of polarization extending usually less than one octave in or close to decimeter range;
UNCLF = unclassified activity.

Solar Geophysical Data classification

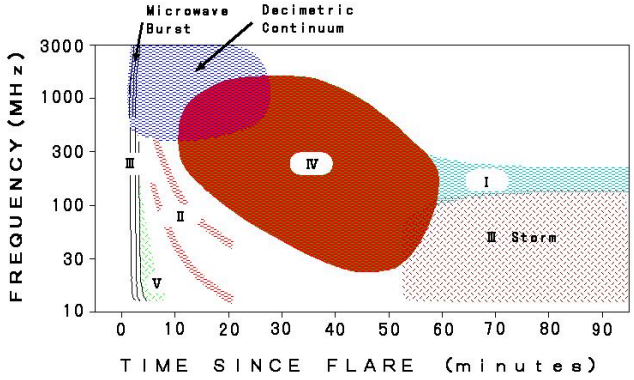

Hiraiso Solar Observatory classification (reversed frequency scale)